ЖЭТФ, 2015, том 148, вып. 6 (12), стр. 1104–1114

ELECTROMAGNETICALLY INDUCED TRANSPARENCY RESONANCES INVERTED IN MAGNETIC FIELD

A. Sargsyan [a], ***D. Sarkisyan*** [a]*, ***Y. Pashayan-Leroy*** [b], ***C. Leroy*** [b], ***S. Cartaleva*** [c], ***A. D. Wilson-Gordon*** [d], ***M. Auzinsh*** [e]

[a] *Institute for Physical Research, NAS of Armenia 0203, Ashtarak-2, Armenia*

[b] *Laboratoire Interdisciplinaire Carnot de Bourgogne, UMR CNRS 6303, Université de Bourgogne, France*

[c] *Institute of Electronics, Bulgarian Academy of Sciences, Sofia, Bulgaria*

[d] *Department of Chemistry, Bar-Ilan University Ramat Gan 5290002, Israel*

[e] *Department of Physics, University of Latvia LV-1586, Riga, Latvia*

Received May 22, 2015

The phenomenon of electromagnetically induced transparency (EIT) is investigated in a Λ-system of the ^{87}Rb D_1 line in an external transverse magnetic field. Two spectroscopic cells having strongly different values of the relaxation rates γ_{rel} are used: an Rb cell with antirelaxation coating ($L \sim 1$ cm) and an Rb nanometric-thin cell (nanocell) with a thickness of the atomic vapor column $L = 795$ nm. For the EIT in the nanocell, we have the usual EIT resonances characterized by a reduction in the absorption (dark resonance (DR)), whereas for the EIT in the Rb cell with an antirelaxation coating, the resonances demonstrate an increase in the absorption (bright resonances (BR)). We suppose that such an unusual behavior of the EIT resonances (i. e., the reversal of the sign from DR to BR) is caused by the influence of an alignment process. The influence of alignment strongly depends on the configuration of the coupling and probe frequencies as well as on the configuration of the magnetic field.

DOI: 10.7868/S0044451015120068

1. INTRODUCTION

In order to observe coherent processes in atomic vapor cells, such as coherent population trapping (CPT), electromagnetically induced transparency (EIT), and electromagnetically induced absorption (EIA), it is important to ensure conditions that allow ground-state coherent spin states to survive many collisions with the cell walls [1–7]. For this purpose, antirelaxation coatings (ARC) can be used in atomic vapor cells [8]. The use of a vapor cell with ARC allows obtaining ultranarrow resonances with the linewidth less than 2 Hz in the nonlinear magneto-optic effect [9]. Ultranarrow EIT resonances of width ~ 100 Hz have been observed in [10] using a vapor cell with ARC. In [11], the transformation of a Ramsey EIA into a magnetic-field-induced transparency resonance in a paraffin-coated Rb vapor cell in the Hanle configuration, with a linewidth of 0.6 mG was reported. The Hanle configuration has also been used to study the ^{87}Rb, D_1 line [12]. The EIT process in multi-Zeeman-sublevel atoms has been considered in [13]. Experimental evidence for the bright magneto-optical resonance sign reversal in Cs atoms confined in a nanocell has been presented in [14]. Margalit et al. have studied the effect of a transverse magnetic field on the absorption spectra of degenerate two-level systems in the D_2 line of ^{87}Rb [15] and degenerate Λ systems in the D_1 line of ^{87}Rb [16].

Here, for the first time to our knowledge, we present

*E-mail: davsark@yahoo.com, david@ipr.sci.am

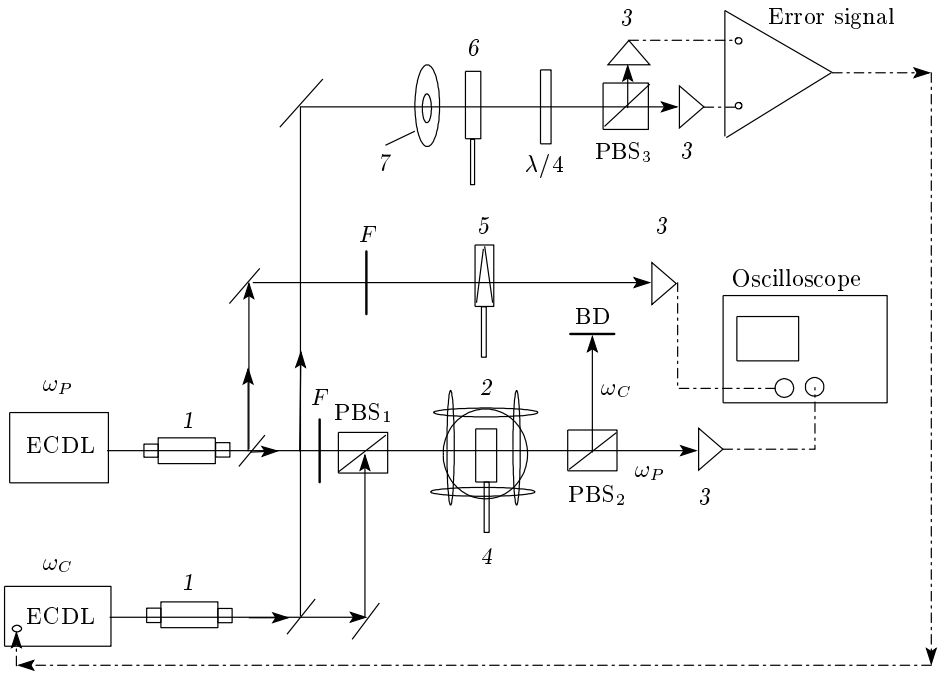

Fig. 1. Sketch of the experimental setup. *1* — Faraday isolators, $PBS_{1,2,3}$ — polarization beam splitters, *2* — Helmholtz coils, *3* — photodiodes, *4* — Rb vapor cell with ARC or Rb nanocell, *5* — auxiliary nanocell with $L = \lambda$, *6* — auxiliary nanocell with $L = \lambda/2$, *7* — permanent ring magnet, BD — beam damp, F — filters

experimental evidence for the transformation of a dark resonance (DR) into a bright resonance in an external transverse magnetic field in a Rb vapor cell with ARC. The results are compared with those obtained using a Rb nanocell with a vapor column of the thickness $L = 795$ nm, where the sign reversal is absent.

2. EXPERIMENT

The experimental arrangement is sketched in Fig. 1. Two beams of single-frequency extended cavity diode lasers (ECDL) with $\lambda \approx 795$ nm (linewidth ~ 1 MHz) are well superposed and directed with the help of a polarization beam splitter PBS_1 either onto the Rb ARC cell, or onto the Rb nanocell. The coupling and probe beams have linear and perpendicular polarizations. The Rb ARC cell or the Rb nanocell (*4*) are placed inside three pairs of mutually perpendicular Helmholtz coils (*2*), making it possibility to cancel the laboratory magnetic field as well as to apply a homogeneous magnetic field. The optical emissions are recorded by photodiodes (*3*) and the signal of the photodiodes is intensified and recorded by digital storage oscilloscope Tektronix TDS 3032B; F are filters. The power of the coupling and probe lasers are 1–30 mW and 5 μW–0.5 mW, respectively. An improved dicroic atomic vapor laser lock (DAVLL) method is used for the coupling frequency stabilization [17]. The frequency reference spectra formation is realized with the help of an auxiliary nanocell with $L = \lambda$ (*5*) [17]. A PBS_2 is used to separate the coupling and probe beams, such that only the probe beam transmission is monitored.

2.1. The coupling is in resonance with the $1 \to 1'$ transition; the probe is scanned through the $2 \to 1'$ transition

In Fig. 2*a*, a Λ-system formed in the ^{87}Rb D_1 line is shown. The coupling frequency is in resonance with the $1 \to 1'$ transition, while the probe frequency is scanned through the $2 \to 1'$ transition (the primes indicate the upper levels of the atoms). Two cells filled with natural Rb are used: an 8 mm long cell with ARC (ARC cell) and a nanocell with the thickness $L = \lambda = 795$ nm [17]. An external magnetic $\mathbf{B}$ field is directed along the probe $\mathbf{E}_P$ field, while $\mathbf{E}_C$ is perpendicular to the $\mathbf{B}$ field (see Fig. 2*b*). In Fig. 3, the EIT spectra for the nanocell (the upper curve) and the ARC cell (the lower curve) are shown for the transverse magnetic field $\mathbf{B} \approx 27$ G. The respective coupling and probe laser

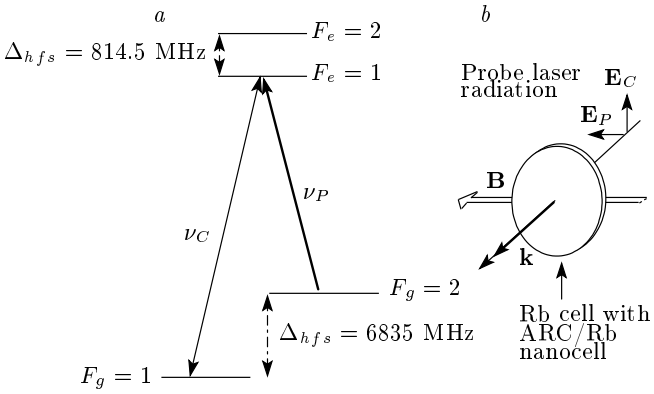

Fig. 2. *a*) Λ-system of the ^{87}Rb D_1 line. *b*) The configuration of **B, k,** $\mathbf{E}_P$, and $\mathbf{E}_C$

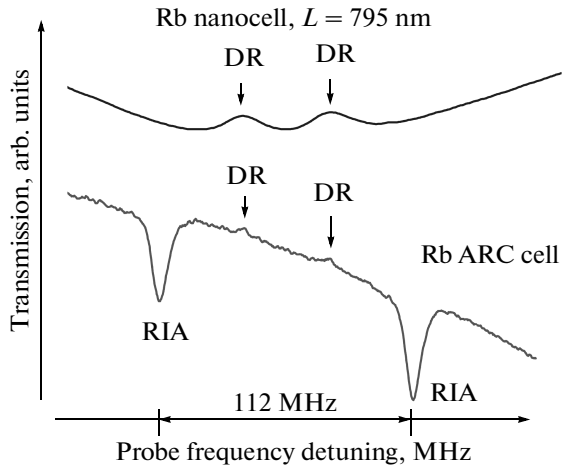

Fig. 3. ^{87}Rb D_1 line. The EIT spectra for the Rb nanocell with $L = \lambda = 795$ nm, $T = 110\,^{\circ}$C (upper curve): two DRs are shown. For the ARC cell, $T = 36\,^{\circ}$C (lower curve) two small DRs and two large RIA are shown. The probe power is 0.2 mW, the coupling power is 13.6 mW, and $B \approx 27$ G

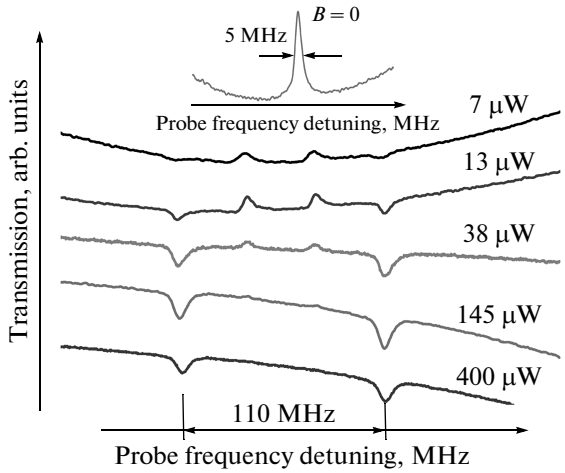

Fig. 4. ^{87}Rb D_1 line, and DR and RIA spectra for the ARC cell ($T = 36\,^{\circ}$C) versus the probe laser power. The coupling laser power is 13.6 mW and $B \approx 27$ G

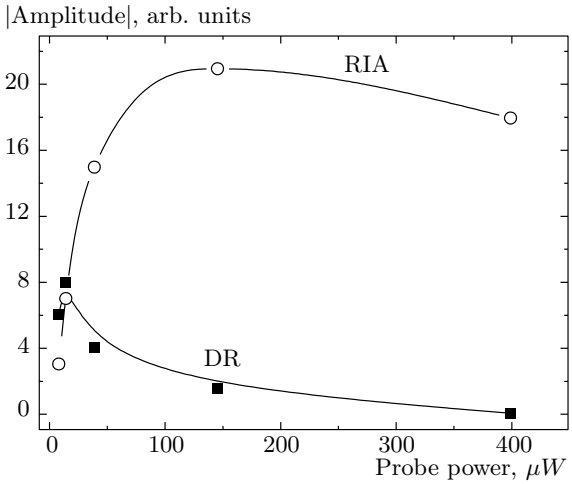

Fig. 5. Dependence of the RIA and DR amplitudes as functions of the probe laser power, $T = 36\,^{\circ}$C and $B \approx 27$ G

powers are 13.6 mW and 0.2 mW. It can be seen that we have the usual EIT resonances for the nanocell, demonstrating a reduction in the absorption (dark resonances). As shown previously [16], there are four DRs. However, it is easy to show that the middle two must be stronger (see Figs. 18 and 20 below). The situation is very different for the ARC cell. There, we see that the two outer high-amplitude resonances show an increase in absorption, i. e., they are bright resonances (we call them resonances inverted by alignment (RIA)). Figure 4 shows the EIT spectra for the ARC cell as a function of the probe laser power for $B \approx 27$ G (the coupling laser power is 13.6 mW). It can be seen that increasing the probe intensity results in the disappearance of the EIT resonance (see also Fig. 5), which can be related to the stronger alignment of atomic population on Zeeman sublevels of the $F_g = 2$ level when the probe intensity is enhanced. The inset shows the DR for $B = 0$, where the linewidth is ~ 5 MHz.

We note that for the respective coupling and probe lasers powers 1mW and 0.01 mW, the linewidth of the DR is 3.5 MHz (but with a smaller contrast). It is well known that in order to obtain narrow DRs, the two lasers must be coherently coupled [3, 4]. However,

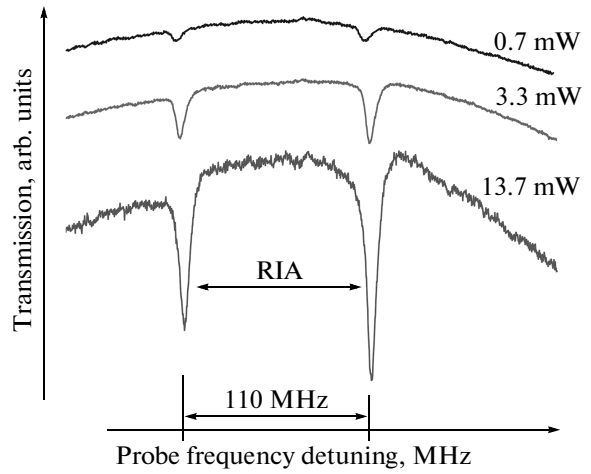

Fig. 6. ^{87}Rb D_1 line, RIA spectra versus the coupling laser power. The probe laser power is 0.5 mW and $B \approx 27$ G

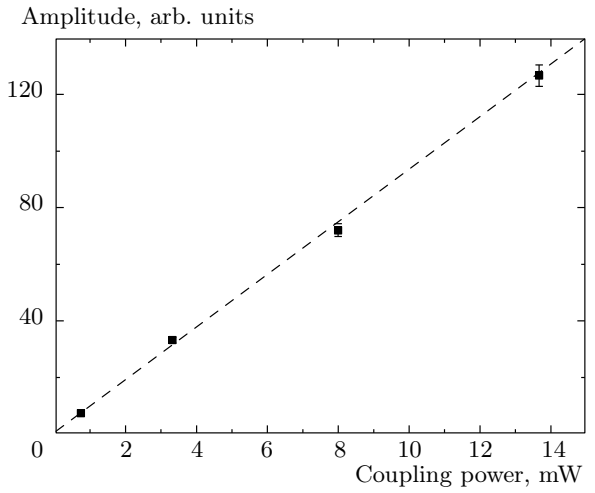

Fig. 7. Dependence of the RIA amplitude on the coupling laser power; the probe laser power is 0.5 mW and $B \approx 27$ G

for the study of the EIT resonance splitting and shift in strong external magnetic fields (when the frequency shift reaches several GHz), a convenient alternative is the use of two different lasers [19]. The dependence of the DR and RIA for the ARC cell as a function of the coupling power (with the probe power 0.5 mW) is shown in Figs. 6 and 7. The enhancement of the amplitude of the RIA resonances with increasing the coupling beam intensity can be attributed to hyperfine optical pumping from the $F_g = 1$ to $F_g = 2$ level due to the coupling laser. As a result, more atoms are redistributed among the $F_g = 2$ Zeeman sublevels due

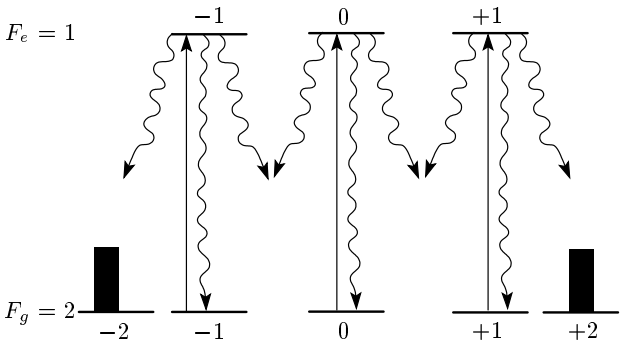

Fig. 8. ^{87}Rb D_1 line, the Zeeman optical pumping process for the $2 \to 1'$ transition (see [20, 21])

to the Zeeman optical pumping (ZOP) process. In order to explain the unusual behavior of the RIA, the transition system in terms of the ZOP for the ^{87}Rb D_1 line $2 \to 1'$ is shown in Fig. 8. Due to the ZOP effect caused by the strong probe beam, the population of the level $F_g = 2$ can be trapped in sublevels with $m_F = \pm 2$ (shown by black bars), which means that so-called alignment occurs [20, 21]. The alignment effect causes a strong redistribution of the population of the $F_g = 2$ level. We note that the population of the outermost Zeeman sublevels with $m_F = \pm 2$ is high also because these levels are not excited by the laser light.

The increase (or reduction) in the population N by ΔN of the levels $F_g = 2$ with $m_F = \pm 2$ is [20, 21]

$$\Delta N \sim \left(\frac{dE_P}{\hbar}\right)^2 \frac{1}{\gamma_N \gamma_{rel}}, \qquad (1)$$

where $dE_P/\hbar$ is the Rabi frequency of the probe laser, γ_N is the natural linewidth, and γ_{rel} is the rate of decay of the coherence between the lower levels. We see from Eq. (1) that ΔN strongly depends on the relaxation rate γ_{rel}. For a usual cell without ARC, it is inversely proportional to the time-of-flight of the atom across the laser beam with a diameter D, and for $D \approx 1$ mm, γ_{rel} is typically ~ 100 kHz. For our ARC cell, it is ~ 1 kHz due to the antirelaxation coating not being of high quality, while an advantage of this ARC cell is its resistance to temperature up to 100 °C [22].

For the nanocell, the relaxation rate is much higher (γ_{rel} is ~ 1 MHz). This is related to the frequent collisions of the Rb atoms with the nanocell windows, destroying the alignment process (see the upper curve in Fig. 3). Figure 9 shows the splitting and the shift of the RIA as a function of the transverse magnetic field B. The frequency interval between the RIAs is ≈ 4.2 MHz/G (see below) and remains linear with B

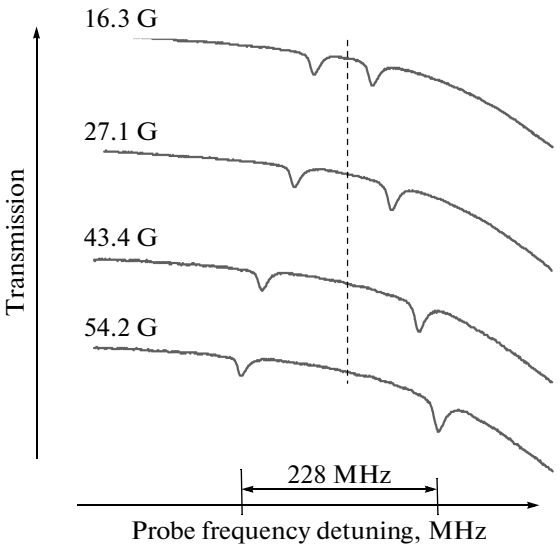

Fig. 9. Splitting and shift of the RIA as functions of the external transverse magnetic B field. The frequency interval between the RIA is ≈ 4.2 MHz/G. The dashed line shows that RIA are displaced symmetrically with respect to the initial position of the DR at $B = 0$

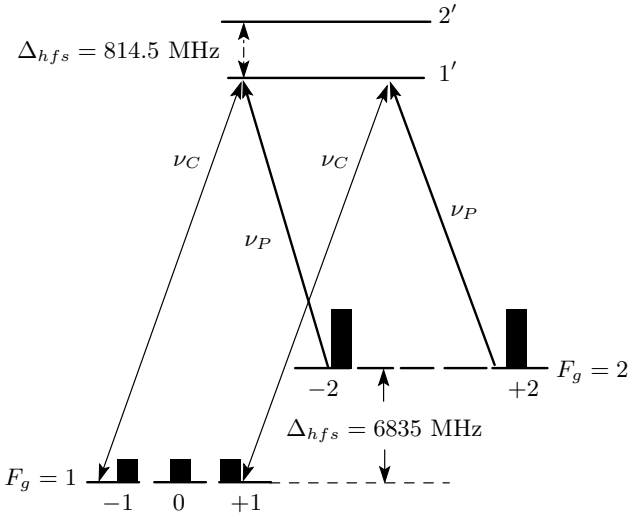

Fig. 10. ^{87}Rb D_1 line, a two-photon Raman-type process. The populations $N(F_g = 2, m_F = \pm 2)$ are indicated by the large bars, and the populations $N(F_g = 1, m_F = \pm 1))$ by the small bars. We suppose that the sublevels $m_F = \pm 2$ of the level $F_e = 2$ are also involved (via the $2 \to 2'$ transition)

up to 100 G. As can be seen, the amplitudes of the RIA are almost independent of the magnetic field.

As regards the physical mechanism of RIA formation, we propose the following. Since there are eight Zeeman sublevels for the $F_g = 1$, 2 levels, initially all the Zeeman sublevels are populated equally, with the population $1/8$ for each sublevel. In the case of a strong ZOP, all the population of $F_g = 2$ is concentrated in the sublevels $m_F = \pm 2$, and hence their population is $5/16$, while the population in the $F_g = 1$ Zeeman sublevels is $2/16$ for each sublevel. Because

$$N(F_g = 2, m_F = \pm 2) > N(F_g = 1, m_F = 0, \pm 1),$$

strong absorption of the probe radiation ν_P can occur via a two-photon Raman-type process (with the emission at the coupling frequency ν_C), shown in Fig. 10. We suppose that the sublevels $m_F = \pm 2$ of the level $F_e = 2$ are also involved (via the $2 \to 2'$ transition) in this two-photon Raman-type process (see Fig. 11). We note that competition between the EIT and a two-photon Raman-type process has been observed for a Λ-system of Na atoms when the probe and coupling laser frequencies were near resonance [23].

A similar process has been considered in a Λ-system of ^{87}Rb, where the ground levels of the system are formed by the Zeeman sublevels of the same ground level [24]. The cross-section for such a two-photon

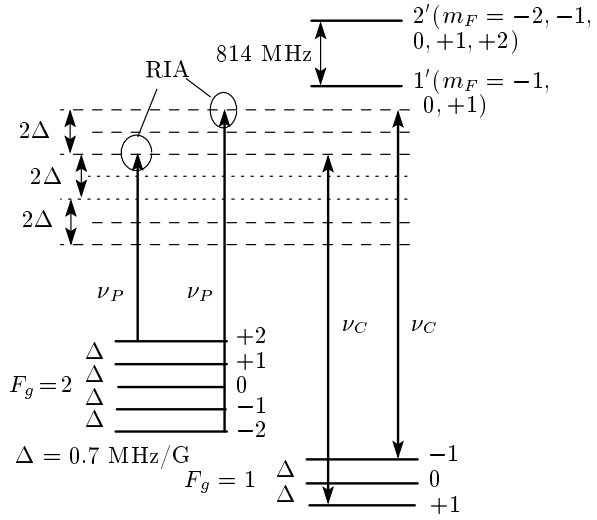

Fig. 11. ^{87}Rb D_1 line, a two-photon Raman-type process. The frequency separation between the RIAs: the coupling laser frequency ν_C (with σ^+ and σ^- polarizations) is fixed, the probe laser frequency ν_P (with the π polarization) is varied. The frequency interval between RIA is $6 \cdot 0.7$ MHz/G $= 4.2$ MHz/G

Raman-type absorption (TPA) process of the probe beam ν_P is

$$\sigma_{TPA} = \frac{\lambda^2}{16\pi^2}\,\frac{\gamma_N}{\gamma_{21}}\left(\frac{dE_C}{\hbar\Delta}\right)^2, \qquad (2)$$

where $dE_C/\hbar$ is the Rabi frequency of the coupling radiation (hence, σ_{TPA} is proportional to the coupling laser power, see Figs. 6 and 7), Δ is the laser frequency detuning from the $5P_{1/2}$ level, $\gamma_N = 6$ MHz, $\gamma_{rel} \approx 0.001$ MHz, and $\lambda = 795$ nm. For TPA of the probe laser radiation, we have $\sigma_{TPA}(N_{g2} - N_{g1})L$, $\Delta \approx 30$–40 MHz, $\Omega_C \approx 35$ MHz, and $L \approx 0.8$ cm. If we suppose that ^{87}Rb $(N_{g2} - N_{g1}) \approx 10^8$ cm^{-3} (which is a realistic number because N (^{87}Rb) $\approx 7 \cdot 10^9$ cm^{-3} at $T = 35\,^\circ$C), then TPA (i. e., RIA) can reach ~ 10 percent, which agrees with the experiment.

The value of the frequency separation between the RIAs is determined by the diagram presented in Fig. 11. The frequency ν_C of the coupling laser (having σ^+ and σ^- polarizations) is fixed, while the frequency ν_P of the probe laser (having π polarization) varies. The first process forming RIA starts from $F_g = 2$, $m_F = +2$ and finishes at $F_g = 1$, $m_F = +1$, while the second process starts from $F_g = 2$, $m_F = -2$ and finishes at $F_g = 1$, $m_F = -1$. We suppose that the sublevels $m_F = \pm 2$ of the level $F_e = 2$ are also involved for the probe radiation (via the 2–2′ transition) by this two-photon Raman-type process, since level 2′ is located ≈ 800 MHz above level 1′, and hence the transitions 2–1′ and 2–2′ overlap by the Doppler wings. We note that it has been demonstrated in [25] for a TPA process (in a ladder system) that even for a 1.5 GHz detuning from the intermediate level, nearly 100 percent absorption is achieved for on Rb 2 mm long cell. A similar situation takes place for the two-photon Raman-type process shown in Fig. 15 below (with the sublevels $m_F = \pm 2$ of the level $F_e = 2$ also involved). As we see, the frequency interval between two RIAs is $6 \cdot 0.7$ MHz/G $= 4.2$ MHz/G. It is easy to show that for the EIT splitting in the case of the nanocell (Fig. 3), the frequency interval between the two neighboring EIT resonances is $2 \cdot 0.7$ MHz/G $= 1.4$ MHz/G.

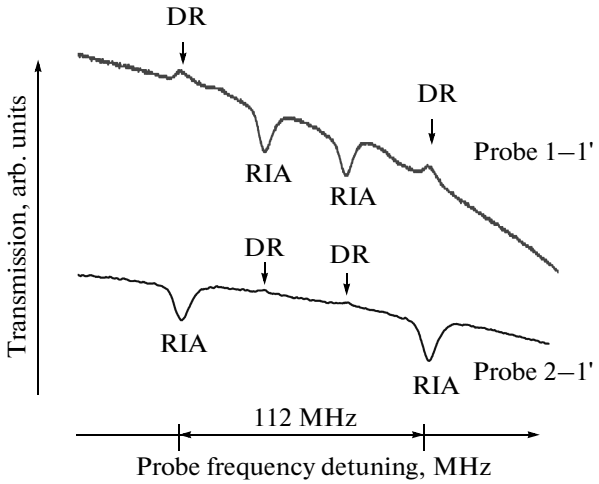

Fig. 12. ^{87}Rb D_1 line, the EIT spectra for the ARC cell, $T = 36\,^\circ$C. The upper curve shows the spectrum for the coupling and probe laser frequency configuration in Fig. 13, and the lower curve refers to the configuration in Fig. 3. The probe power is 0.2 mW, the coupling power is 13.6 mW, and $B \approx 27$ G

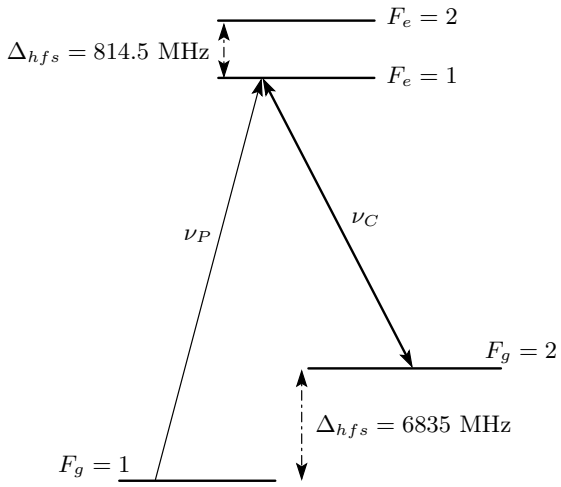

Fig. 13. Λ-system of the ^{87}Rb D_1 line

2.2. The coupling is in resonance with the $2 \to 1'$ transition; the probe is scanned through the $1 \to 1'$ transition

Figure 12 presents the transmission spectra for the ARC cell at $T = 36\,^\circ$C. The upper curve shows the spectrum for the coupling and probe laser frequency configuration presented in Fig. 13, while the lower curve corresponds to the configuration of ν_C and ν_P presented in Fig. 3. It is important to note that when the probe laser power is increased, DRs (shown in the upper curve) are still present in the spectrum, while in the lower curve, the DRs completely vanish for a power > 0.4 mW (only the two RIAs remain). Therefore, we suppose that the alignment process illustrated in Fig. 14 does not lead to the complete depletion of the $m_F = \pm 1$ Zeeman sublevels of the ground state. Probably, this can be related to the hyperfine optical pumping by the coupling laser to the $F_g = 1$ level. Due to the ZOP effect caused by the probe laser in the $1 \to 1'$ Zeeman sublevel system, the main population of the level

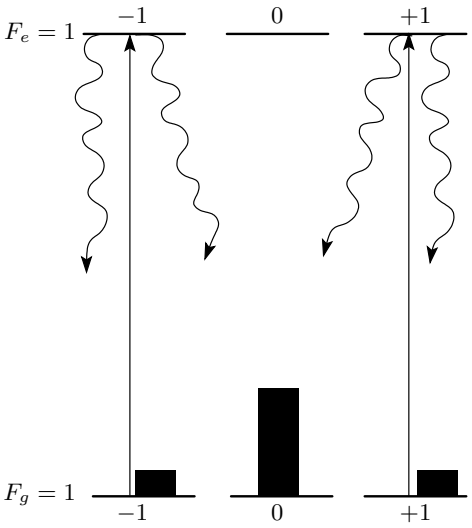

Fig. 14. ^{87}Rb D_1 line, the Zeeman optical pumping process for the $1 \to 1'$ transition [20, 21]

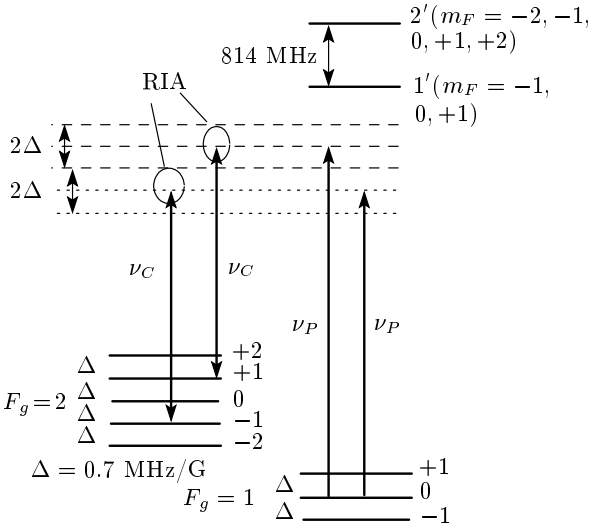

Fig. 15. ^{87}Rb D_1 line, a two-photon Raman-type process. The coupling laser contains σ^+ and σ^- polarizations and its frequency ν_C is fixed, the probe laser has the frequency ν_P that is varied and has a π polarization. As we see, the frequency interval between RIA for the upper curve presented in Fig. 12 is 1.4 MHz/G

$F_g = 1$ in the case of a strong probe laser is concentrated in the sublevels $m_F = 0$ (shown with the black bar) [20, 21]. The value of the frequency separation between the RIAs is determined by the diagram presented in Fig. 15. The coupling laser frequency ν_C is fixed, while the probe laser frequency ν_P is varied and has a π polarization. The first process forming RIA starts

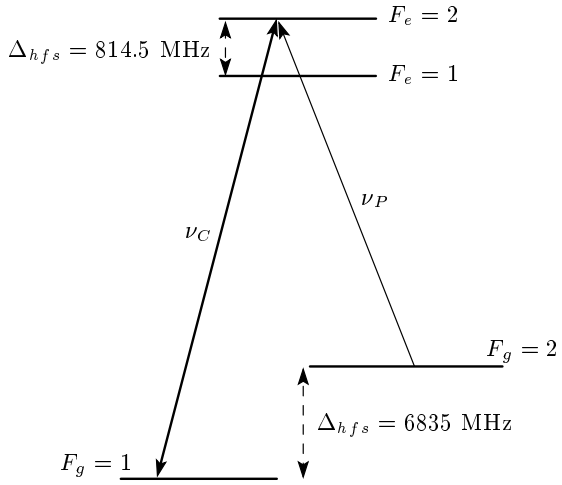

Fig. 16. Λ-system of the ^{87}Rb D_1 line

from $F_g = 1$, $m_F = 0$ and finishes at $F_g = 2$, $m_F = +1$, while the second process starts from $F_g = 1$, $m_F = 0$ and finishes at $F_g = 2$, $m_F = -1$. We note that the RIA resonance formation starts from the most populated Zeeman sublevel of the $F_g = 1$ hyperfine level, which is $m_F = 0$ (see Fig. 14). Thus, both RIA resonances (Fig. 12, the upper spectrum) are situated in the middle, between the DRs. For good DR formation, the atomic population of ground levels in the Λ-system has to be similar. By contrast, the RIA resonance is well pronounced when there is a large population difference between the ground levels. Thus, the spectrum presented in Fig. 12 (the lower spectrum) can be explained by the fact that, here, the most populated Zeeman sublevels of the $F_g = 2$ level are $m_F = \pm 2$. Consequently, the DRs are between the RIA resonances. As we see, the frequency interval between two RIAs (the upper spectrum) is $2 \cdot 0.7$ MHz/G $= 1.4$ MHz/G.

2.3. The coupling is in resonance with the $1 \to 2'$ transition; the probe is scanned through the $2 \to 2'$ transition

The Λ^{87}Rb system of the D_1 line is shown in Fig. 16. Figure 17 shows the EIT and RIA spectra for the nanocell, $L = \lambda = 795$ nm (the upper curve) and the ARC cell (the lower curve), for the transverse magnetic field $B \approx 27$ G. The respective coupling and probe laser powers are 13.6 mW and 0.2 mW. As can be seen for the EIT spectrum in the nanocell, all four narrow features represent usual DRs characterized by a reduction in the absorption. Under similar conditions in the case of the ARC cell, the two DRs are of reversed sign, i. e., the RIA resonances that show increased absorption. The

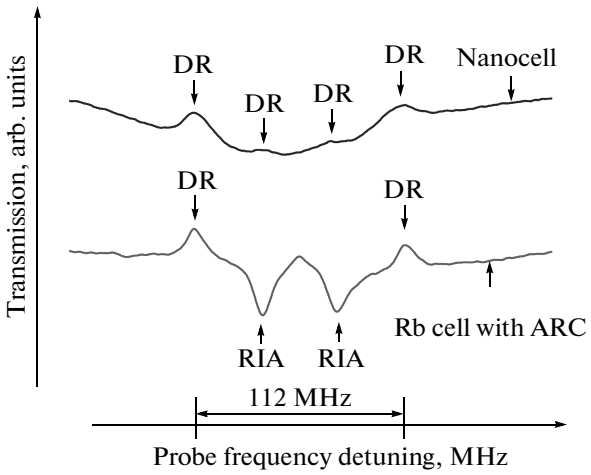

Fig. 17. ^{87}Rb D_1 line, the EIT spectra for the Rb nanocell, $L = \lambda = 795$ nm, $T = 110\,^{\circ}$C (upper curve) and for the Rb ARC cell, $T = 36\,^{\circ}$C (lower curve); the probe laser power is 0.2 mW, the coupling laser power is 13.6 mW, and $B \approx 27$ G

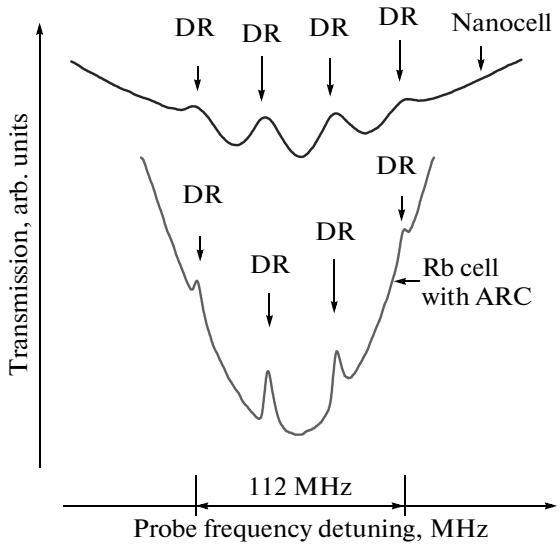

Fig. 18. ^{87}Rb D_1 line, the EIT spectra for the nanocell, $L = \lambda = 795$ nm, $T = 110\,^{\circ}$C (upper curve) and for the ARC cell, $T = 36\,^{\circ}$C (lower curve). The probe laser power is 0.2 mW, the coupling laser power is 13.6 mW, and $B \approx 27$ G

frequency interval between the two RIAs in the lower curve in Fig. 17 is $2 \cdot 0.7$ MHz/G $= 1.4$ MHz/G. Here, the ZOP results in a strong population accumulation in the $F_g = 2$, $m_F = 0$ Zeeman sublevel. Thus, the situation is similar to that presented in Figs. 12 and 14, and the RIA resonances are situated between the DRs.

2.4. The coupling is in resonance with the $2 \to 2'$ transition; the probe is scanned through the $1 \to 2'$ transition

This case is interesting because it differs from the previously presented results. Figure 18 (the upper curve) shows that there are only EIT resonances in the spectrum, for the nanocell with $L = \lambda = 795$ nm. All DRs have good amplitudes, which can be related to the small value of the Zeeman sublevel population redistribution due to the alignment process. In Fig. 18 (the lower curve), the case of using the ARC cell at the transverse magnetic field $B \approx 27$ G is presented for the configuration shown in Fig. 19 and the respective coupling and probe laser powers 13.6 mW and 0.2 mW. As we see, it is only for this particular configuration that the EIT spectra, both for the nanocell and the ARC cell, have the usual EIT resonances characterized by a reduction in absorption. The frequency interval between the neighboring EITs (see Fig. 20) is $2 \cdot 0.7$ MHz/G $= 1.4$ MHz/G. For this energy level configuration and magnetic field, the transitions between

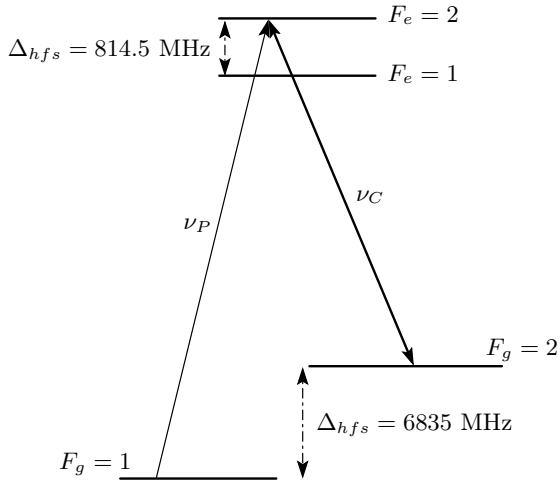

Fig. 19. Λ-system of the ^{87}Rb D_1 line

Zeeman sublevels of the $F_g = 1 \leftrightarrow F_e = 2$ hyperfine transition results in the alignment of atomic population of the Zeeman sublevels belonging to the $F_g = 1$ level. But in this configuration, all Zeeman sublevels of the $F_g = 1$ level are excited by the probe light beam, and it is therefore impossible to achieve strong ZOP, thereby creating conditions for the RIA resonance formation.

We note that in [18], the results for EIT in a magnetic field are presented for the ^{87}Rb D_1 line for the

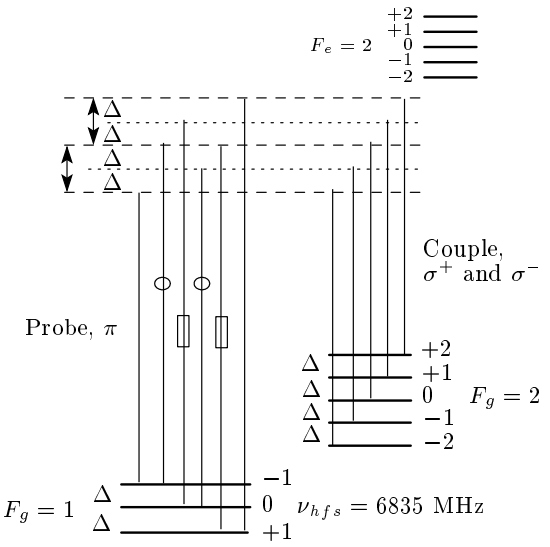

Fig. 20. ^{87}Rb D_1 line, a two-photon Raman-type process. The coupling laser has a fixed frequency ν_C and σ^+ and σ^- polarizations, the probe laser has the π polarization, and the frequency ν_P is varied. Degenerate frequencies are indicated by circles and rectangles. There are four different EIT frequencies. The frequency interval between the neighboring EITs is $2 \cdot 0.7$ MHz/G $= 1.4$ MHz/G

ν_C and ν_P configuration in Fig. 19, and there are also four EIT resonances, as shown in Fig. 18. However, the diagram shown in Fig. 1 in [18] is incorrect because the coupling laser frequency varies, rather than being constant as shown in Fig. 20.

3. DISCUSSIONS AND CONCLUSION

As we see from the results presented above, the most convenient Λ-system for the RIA observation is the one shown in Fig. 2*a*, where ν_C is in resonance with the $1 \to 1'$ transition, while ν_P is scanned through the $2 \to 1'$ transition. We suppose that in this case (the configuration shown in Fig. 2*b*), the alignment is very effective due to the strong Zeeman optical pumping. For the other ν_C and ν_P configurations, the alignment is weaker, which is probably caused by an additional redistribution of the population between the Zeeman sublevels caused by the strong coupling laser.

In order to demonstrate that the alignment process (shown in Fig. 6) is caused by the probe laser with the π polarization, we have studied another experimental configuration shown in Fig. 21. The EIT spectrum for the ARC cell and the magnetic field $B \approx 27$ G is the lower spectrum shown in Fig. 22, while the upper spectrum shows the DRs for B =0. As we can see, the spectrum is very different from that presented in Fig. 3: instead of the RIAs, we have four DRs characterized by a reduction in the absorption (the two middle DRs have dispersion-like profiles that probably demonstrate the competition between EIT and TPA).

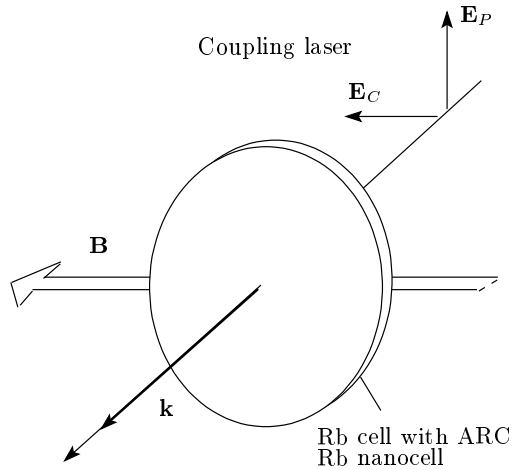

Fig. 21. The configuration of $\mathbf{B}$, $\mathbf{k}$, $\mathbf{E}_P$, and $\mathbf{E}_C$

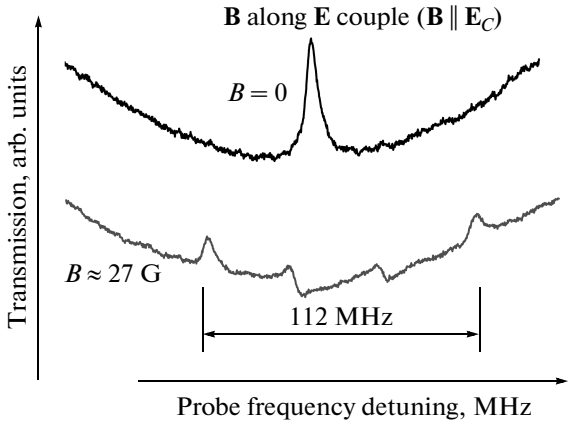

Fig. 22. ^{87}Rb D_1 line, the EIT spectra for the ARC cell, $T = 36\,^\circ$C. The respective coupling and probe laser powers are 13.6 mW and 1 mW. The upper spectrum shows the EIT resonance for $B = 0$, and the lower spectrum shows the EIT spectrum for $\mathbf{B} \parallel \mathbf{E}_C$, with $B \approx 27$ G

Also, using the ν_C and ν_P configuration shown in Fig. 2*a*, and applying a longitudinal magnetic field ($\mathbf{B} \parallel \mathbf{k}$), we have detected the well-known spectrum with three DRs shown in Fig. 23. In this case, the magnetic field creates three Λ-systems (shown in the inset) and three DRs are formed [3, 16, 26]. The middle DR has a larger amplitude, since there are two channels

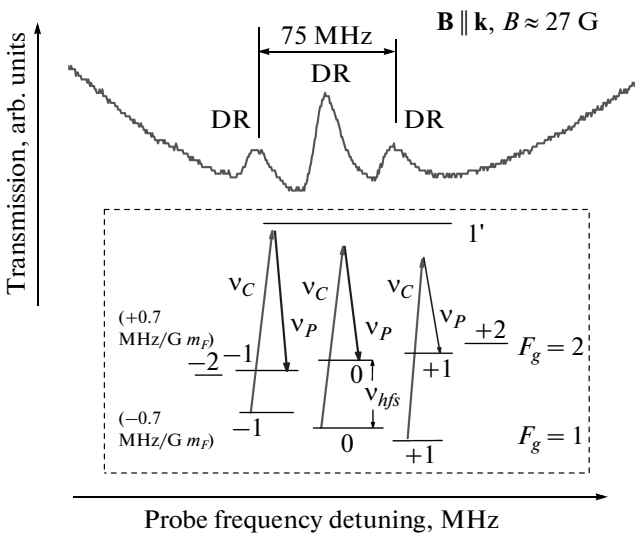

Fig. 23. ^{87}Rb D_1 line, the EIT spectra for the ARC cell, $T = 36\,^{\circ}$C. The respective coupling and probe laser powers are 13.6 mW and 1 mW, and a longitudinal magnetic field $\mathbf{B} \parallel \mathbf{k}$, $B \approx 27$ G is applied. Three DRs are shown. The inset shows three Λ-systems formed by the magnetic field

for its formation when the probe and coupling lasers have polarizations (σ^+, σ^-) or (σ^-, σ^+) and they form the middle DR with the same frequency. The identical three DRs are also formed in the nanocell with $L = 795$ nm [17].

From the systematic experimental study reported here, it can be concluded that the good-amplitude RIA resonances are observed in the case of strong alignment enabled by the probe beam and low Zeeman optical pumping by the coupling laser.

It is well known that velocity-selective optical pumping (VSOP) resonances accompany the EIT (DR) resonances [27]. In the case of EIT in an atomic vapor cell with ARC (see Figs. 3, 9, 12, 17, 18, 22 and Fig. 23), these VSOPs have a very small amplitude or are absent.

A simple practical method to measure the quality of the ARC is presented in [28], which is based on the measurement of the temporal dependence of the intensity of the fluorescence from irradiated alkali atoms by pulsed light at resonance. We note that the results presented in Fig. 4 can also be used for testing the ARC quality, i. e., to determine the number of collisions $N_C(\text{surv})$ with the cell walls that is sufficient for the ground-state coherent spin states to survive. As we see for the probe laser power of 13 μW, the ratio of the amplitudes is $|A(\text{RIA})/A(\text{DR})| \approx 1$. If $N_C(\text{surv})$ is larger than that used for the ARC cell ($N_C(\text{surv}) \approx 200$–$300$), then the ratio is > 1 at the same probe laser power of 13 μW.

This work was partially supported by a Marie Curie International Research Staff Exchange Scheme Fellowship within the 7th European Community Framework Programme "Coherent optics sensors for medical applications-COSMA" (Grant Agreement No: PIRSES-GA-2012-295264) and in the scope of the International Associated Laboratory IRMAS (CNRS-France & SCS-Armenia).

REFERENCES

1. G. Alzetta, A. Gozzini, L. Moi, and G. Orriols, Nuovo Cim. Soc. Ital. Fis. B **36**, 5 (1976).
2. S. Harris, Phys. Today **50**, 36 (1997).
3. R. Wynands and A. Nagel, Appl. Phys. B **68**, 1 (1999).
4. M. Fleischhauer, A. Imamoglu, and J. P. Marangos, Rev. Mod. Phys. **77**, 633 (2005).
5. C. Andreeva, S. Cartaleva, Y. Dancheva, V. Biancalana, A. Burchianti, C. Marinelli, E. Mariotti, L. Moi, and K. Nasyrov, Phys. Rev. A **66**, 012502 (2002).
6. S. Knappe, L. Hollberg, and J. Kitching, Opt. Lett. **29**, 388 (2004).
7. Y. Pashayan-Leroy, C. Leroy, A. Sargsyan, A. Papoyan, and D. Sarkisyan, J. Opt. Soc. Amer. B **24**, 1829 (2007).
8. M. A. Bouchiat and J. Brossel, Phys. Rev. **147**, 41 (1966).
9. D. Budker, V. Yashchuk, and M. Zolotorev, Phys. Rev. Lett. **81**, 5788 (1998).
10. M. Klein, M. Hohensee, D. F. Phillips, and R. L. Walsworth, Phys. Rev. A **83**, 013826 (2011).
11. H. S. Moon and H.-J. Kim, Opt. Express **22**, 18605 (2014).
12. S. Cartaleva, G. Alzetta, Y. Dancheva, Ch. Andreeva, and R. M. Celli, Bulgarian J. Phys. **27**, 21 (2000).
13. B. Wang, Y. Han, J. Xiao, X. Yang, Ch. Zhang, H. Wang, Min Xiao, and K. Peng, Phys. Rev. A **75**, 051801-R (2007).
14. C. Andreeva, A. Atvars, M. Auzinsh, K. Blush, S. Cartaleva, L. Petrov, and D. Slavov, Phys. Rev. A **76**, 063804 (2007).

15. L. Margalit, M. Rosenbluh, and A. D. Wilson-Gordon, Phys. Rev. A **87**, 033808 (2013).

16. L. Margalit, M. Rosenbluh, and A. D. Wilson-Gordon, Phys. Rev. A **88**, 023827 (2013).

17. A. Sargsyan, C. Leroy, Y. Pashayan-Leroy, R. Mirzoyan, A. Papoyan, and D. Sarkisyan, Appl. Phys. B **105**, 767 (2011).

18. X. Wei, J. Wu, G. Sun, Z. Shao, Z. Kang, Y. Jiang, and J.-Y. Gao, Phys Rev. A **72**, 023806 (2005).

19. A. Sargsyan, R. Mirzoyan, T. Vartanyan, and D. Sarkisyan, Zh. Eksp. Teor. Fiz. **145**, 414 (2014) [JETP, **118**, 359 (2014)].

20. M. Auzinsh, D. Budker, and S. M. Rochester, *Optically Polarized Atoms: Understanding Light-Atom Interactions*, Oxford Univ. Press, Oxford (2010).

21. D. Budker, D. F. Kimball, and D. P. DeMille, *Atomic Physics*, Oxford Univ. Press, Oxford (2004).

22. S. Gozzini and A. Lucchesini, Europ. Phys. J. D **28**, 157 (2004).

23. V. Wong, R. S. Bennink, A. M. Marino, R. W. Boyd, C. R. Stroud, Jr., and F. A. Narducci, Phys. Rev. A **70**, 053811 (2004).

24. R. Meshulam, T. Zigdon, A. D. Wilson-Gordon, and H. Friedmann, Opt. Lett. **32**, 2318 (2007).

25. A. Sargsyan, M. G. Bason, D. Sarkisyan, A. K. Mohapatra, and C. S. Adams, Opt. Spectrosc. **109**, 529 (2010).

26. L. Margalit, M. Rosenbluh, and A. D. Wilson-Gordon, Phys. Rev. A **85**, 063809 (2012).

27. A. Sargsyan, D. Sarkisyan, D. Staedter, and A. M. Akulshin, Opt. Spectrosc. **101**, 762 (2006).

28. K. Nasyrov, V. Entin, N. Nikolov, N. Petrov, and S. Cartaleva, Proc. SPIE **9447**, 944704 (2015).